Longitudinal In-Vivo X-Ray Fluorescence Computed Tomography With Molybdenum Nanoparticles

Kian Shaker, Carmen Vogt, Yurika Katsu-Jiménez, Raoul V. Kuiper, Kenth Andersson, Yuyang Li, Jakob C. Larsson, Aida Rodriguez-Garcia, Muhammet S. Toprak, Marie Arsenian-Henriksson, and Hans M. Hertz

***Abstract*— X-ray fluorescence computed tomography (XFCT) with nanoparticles (NPs) as contrast agents shows potential for molecular biomedical imaging with higher spatial resolution than present methods. To date the technique has been demonstrated on phantoms and mice, however, parameters such as radiation dose, exposure times and sensitivity have not yet allowed for high-spatial-resolution *in vivo* longitudinal imaging, i.e., imaging of the same animal at different time points. Here we show *in vivo* XFCT with spatial resolution in the 200-400 μm range in a proof-of-principle longitudinal study where mice are imaged five times each during an eight-week period following tail-vein injection of NPs. We rely on a 24 keV x-ray pencil-beam-based excitation of in-house-synthesized molybdenum oxide NPs (MoO_2) to provide the high signal-to-background x-ray fluorescence detection necessary for XFCT imaging with low radiation dose and short exposure times. We quantify the uptake and clearance of NPs *in vivo* through imaging, and monitor animal well-being over the course of the study with support from histology and DNA stability analysis to assess the impact of x-ray exposure and NPs on animal welfare. We conclude that the presented imaging arrangement has potential for *in vivo* longitudinal studies, putting emphasis on designing biocompatible NPs as the future focus for active-targeting preclinical XFCT.**

Manuscript received March 13, 2020; revised May 25, 2020; accepted June 30, 2020. Date of publication July 6, 2020; date of current version November 30, 2020. This work was supported by the Knut and Alice Wallenberg Foundation and the Swedish Cancer Society. *(Corresponding authors: Kian Shaker; Hans M. Hertz.)*

Kian Shaker, Carmen Vogt, Kenth Andersson, Yuyang Li, Jakob C. Larsson, Muhammet S. Toprak, and Hans M. Hertz are with the Department of Applied Physics, KTH Royal Institute of Technology/Albanova, 106 91 Stockholm, Sweden (e-mail: kiansd@kth.se; carmenma@kth.se; kenthan@kth.se; yuyangli@kth.se; jakob.larsson@biox.kth.se; toprak@kth.se; hertz@biox.kth.se).

Yurika Katsu-Jiménez, Aida Rodriguez-Garcia, and Marie Arsenian-Henriksson are with the Department of Microbiology, Tumor and Cell Biology (MTC), Karolinska Institutet, 171 77 Solna, Sweden (e-mail: yurika.katsu@ki.se; aida.rodriguez.garcia@ki.se; marie.arsenian.henriksson@ki.se).

Raoul V. Kuiper is with the Department of Laboratory Medicine, Karolinska Institutet, 141 57 Huddinge, Sweden (e-mail: raoul.kuiper@ki.se).

This article has supplementary downloadable material available at https://ieeexplore.ieee.org, provided by the authors.

Color versions of one or more of the figures in this article are available online at https://ieeexplore.ieee.org.

Digital Object Identifier 10.1109/TMI.2020.3007165

***Index Terms*— Biomedical imaging, computed tomography (CT), in vivo, molecular imaging, nanoparticles, preclinical imaging, X-ray fluorescence computed tomography (XFCT).**

I. Introduction

X-RAY fluorescence (XRF) computed tomography (XFCT) with nanoparticles (NPs) as contrast agents is an emerging biomedical imaging technology, presently focused on preclinical applications but with a clinical outlook. It combines the penetration depth and spatial resolution generic for x-rays with the potential for molecular or functional targeting inherent to NP contrast agents. Among the preclinical imaging modalities [1] XFCT thus belongs to the group of molecular/functional imaging technologies [2], presently dominated by PET (positron emission tomography), SPECT (single photon emission computed tomography), and optical fluorescence and luminescence methods. Here XFCT has potential to provide a spatial resolution an order of magnitude better [3], [4] than the present few-mm range of these methods [2] and with the additional benefit of increased contrast flexibility from the NPs, including the possibility for multiplexing [5].

Nanoparticles are emerging as attractive new contrast agents in biomedical imaging due to their capacity to carry a large payload for higher sensitivity and since they allow complex and flexible tailoring of both physical and biochemical properties for targeted contrast [6]. Targeting can be either active or passive. To date NPs have demonstrated successful *in vivo* preclinical imaging with magnetic, optical, acoustic, and nuclear detection schemes [6]. Nanoparticles have also been investigated as new contrast agents in classical absorption-based x-ray imaging such as computed tomography (CT), with passive targeting [7]–[9] as well as with actively targeted gold NPs against, e.g., lymph nodes (anti-CD4) [10] or breast tumors (HER2) [11]. Other applications of tailored NPs include drug delivery and therapy [12], [13].

X-ray fluorescence (XRF) provides a sensitive means for elemental detection via the characteristic line emission from, e.g., NPs. In contrast to optical methods based on fluorescence [14] or bioluminescence [15], x-rays have the advantage of a much larger penetration depth in combination with no interference from visible-light background such as tissue

autofluorescence, making XRF more suitable as a contrast mechanism for whole-body imaging. Extended to a tomographic technique, XFCT has the potential to quantify the 3D spatial distribution of NPs in small-animals. During the last decade XFCT based on laboratory sources has been investigated for NP bio-imaging [16]. Different data acquisition strategies have been proposed; the scanning pencil-beam geometry [3], [4], [17], [18], full-field excitation combined with a collimated detector [19] or approaches utilizing pinholes for parallel acquisition [20]–[22]. The parallel methods have potential for shorter exposure times while the pencil-beam geometry typically provides higher spatial resolution and lower radiation dose. Common for all strategies is the ability to simultaneously acquire x-ray transmission images resulting in absorption CT at no extra cost (radiation dose, time etc.). The methods have been primarily demonstrated on phantoms. XFCT of mice has been demonstrated *ex vivo* with Au [19] NPs with low spatial resolution and Mo NPs [4] with high spatial resolution. Recently, proof-of-principle *in vivo* experiments have demonstrated promising results with Gd [21] and Au [22] NPs. However, these arrangements present imaging with low spatial resolution and lacking sensitivity. Additionally, experiments have been non-recovery, meaning that XFCT with low radiation dose that allow for longitudinal imaging (i.e., repeated imaging of the same animal over longer periods of time) has yet to be shown.

Here we demonstrate few-100-μm-range spatial resolution *in vivo* XFCT of mice in a proof-of-principle eight-week longitudinal study where mice were imaged 5 times each. We combine our laboratory pencil-beam arrangement and its sensitive XRF detection with tailored MoO_2 NPs and real-time monitoring of respiration and body temperature under anesthesia. The key issues for *in vivo* XFCT imaging are radiation dose, exposure times, and possible other adverse effects on animal well-being arising from NP exposure. Our longitudinal study demonstrates that XFCT can be performed with acceptable scan times and with radiation dose well below typical levels for *in vivo* micro-CT. Furthermore we evaluated the clearance of NPs *in vivo* through imaging and assessed animal well-being throughout the whole study. No signs of abnormalities in animal health were observed during the course of the study, however, histology of extracted organs showed signs of local thrombus formation in mice injected with NPs. This is a known complication of NPs that can be addressed by different means, nevertheless, we note that further studies on the stability and hemocompatibility of the NPs will provide a better understanding of the aggregation and dissolution of the NPs in the living organism. Finally, we use the results to discuss the future of laboratory XFCT, including actively targeted NPs, and requirements for 100-μm spatial resolution *in vivo* imaging.

II. Methods

A. Laboratory XFCT

Fig. 1a shows a schematic of our laboratory XFCT arrangement used for *in vivo* small-animal imaging. A liquid-metal-jet microfocus source (D2, Excillum AB, Sweden) coupled to a W-C-coated multilayer Montel mirror (ELM61, Incoatec GmbH, Germany) acts as our x-ray pencil-beam. The microfocus source operates at 120 kV and 170 W, emitting broadband bremsstrahlung in addition to characteristic line emissions from the liquid-metal anode alloy components Ga (K_α: 9.3 keV), In (K_α: 24.1 keV) and Sn (K_α: 25.3 keV). The multilayer mirror has a Gaussian reflectance profile centered at 24 keV with a full-width-at-half-maximum (FWHM) of $\sim$1.4 keV creating a semi-monochromatic pencil-beam using the 24.1 keV In K_α emission line (see Suppl. Fig. 1). In addition, the mirror reflects low-energy x-rays in the Ga K_α emission range which are filtered out by placing 240 μm of aluminium immediately after the mirror. Single-reflections in the mirror resulting in line-focus are blocked using an aperture with a diameter of 1 mm placed 10 cm after the mirror. The pencil-beam focus diameter is $\sim$100 μm (see Suppl. Fig. 2) with a beam divergence of $\sim$1.8 mrad. The 24 keV flux at the focus was measured to $2.8 \cdot 10^7$ ph/s. Mice to be imaged are placed in the stationary pencil-beam focus, mounted on motorized stages allowing for translation and rotation for acquiring projection images of the mice pixel-by-pixel. See Suppl. Fig. 3 for photographs of the laboratory XFCT arrangement.

Due to the spectral characteristics of the pencil-beam, molybdenum with its K-absorption edge at 20 keV was chosen as the core material of our NPs, acting as the XRF contrast agent. Molybdenum emits K_α XRF at 17.4 keV allowing high signal-to-background detection of XRF photons due to the significant spectral separation from the $>$23 keV main Compton scattering peak (see Fig. 1b).

XRF photons are detected at 90° relative to the pencil-beam at a distance of 25 mm from the focus using a custom 3-element photon-counting silicon-drift detector (SDD, RaySpec Ltd, GB) in a curved housing with a total detection area of 165 mm^2, sensor thickness of 450 μm and energy resolution of $\sim$200 eV at the Mo K_α energy. X-rays transmitted through the mice are measured using a separate 40 mm^2 active area SDD with the same sensor thickness (RaySpec Ltd, GB). 5 mm of aluminium is placed in front of the transmission detector to filter and reduce the incident flux to comply with the count rate limitations of the detector. Synchronized read-out electronics (xMap, XIA LLC, US) allow for dead-time-free and co-registered acquisition of pixels in the XRF and transmission projection images, recorded using in-house acquisition software written in LabView (National Instruments, US) which incorporates the motorized stages. As all detectors are photon-counting, each acquired pixel contains a full spectrum of the x-ray photons detected during the pixel exposure. The x-ray spectra are not affected by pile-up and similar effects due to measurements being carried out well below the maximum input count rate of the read-out electronics ($\sim$1 Mcps). Pixels in horizontal lines are recorded under continuous translation, while overhead (typically $\sim$25%) is introduced in vertical transitions to the next horizontal line as well as rotations between projections

Typical acquisition settings are 200 μm step sizes with 10 ms exposure time per step, where the latter was chosen to balance sensitivity with overall acquisition time.

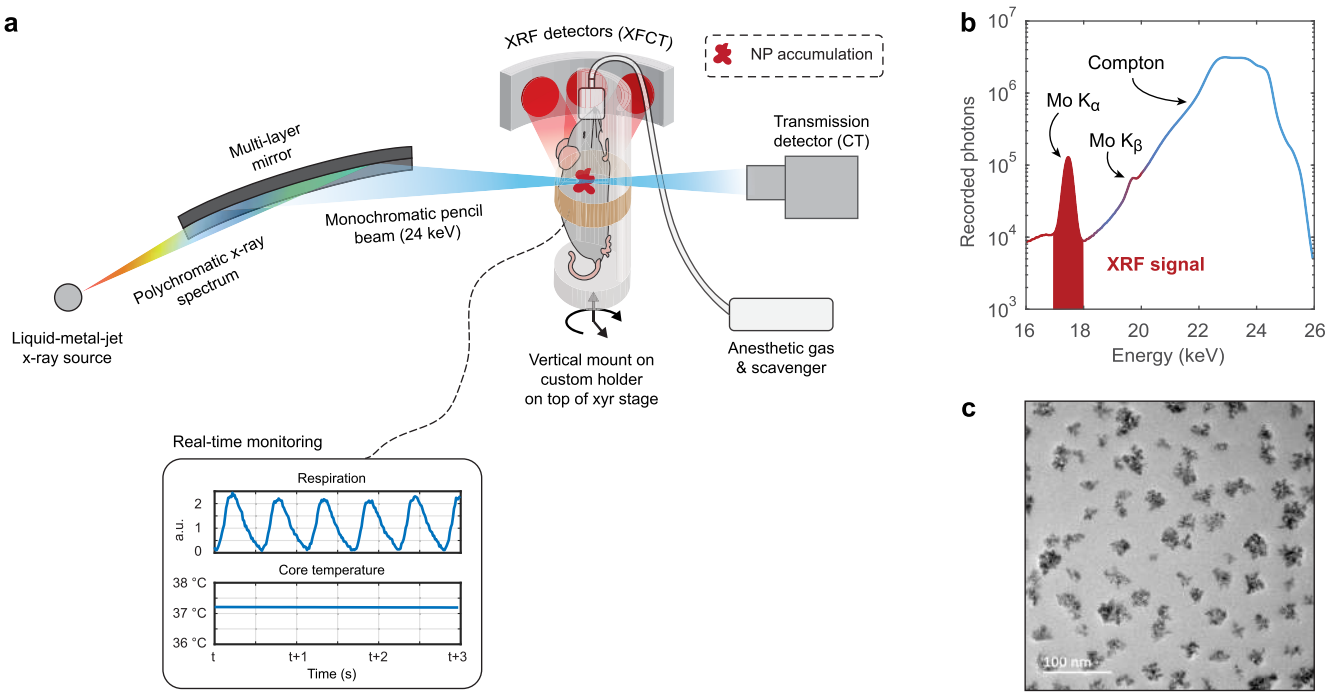

Fig. 1. Experimental arrangement for *in vivo* small-animal XFCT. **a**, Schematic of the imaging arrangement. High-brightness x-ray emission from a liquid-metal-jet source is spatially and spectrally shaped using a multilayer mirror into a pencil-beam used to excite accumulations of MoO_2 NPs injected intravenously in mice. XRF emitted from excited NPs is recorded using a 3-element photon-counting detector on the side. The transmitted x-rays are detected for simultaneous absorption CT. The mice are kept under anesthesia in a custom-made vertical bed while subject to real-time monitoring of respiration and body temperature (graphs shown are experimental data). Motorized stages allow for translating the mice over the stationary pencil-beam to acquire XRF and transmission projection images pixel-by-pixel and at different viewing angles for XFCT and absorption CT. **b**, Example of a recorded spectrum from the XRF detectors, integrated over all pixels from a tomography of a mouse injected with MoO_2 NPs. The 17.4 keV Mo K_α peak is extracted as the XRF signal. The spectrum displayed here is integrated over the 3 angularly separated detector elements, which due to the anisotropy of Compton scattering explains the observed broadening of the Compton peak. **c**, Transmission electron micrograph (TEM) of the MoO_2 NPs. The NPs self-assemble in clusters coated with polyvinylpyrrolidone (PVP).

For tomographic scans typically 30 projections (XRF and transmission) are acquired over 180° allowing for XFCT & CT reconstruction. Total acquisition time depends on the size of the area (2D) or volume (3D) to be imaged. With the settings described above, a whole-body projection image with a size of 40 × 70 mm (200 × 200 μm pixels, cf. Fig. 2a) takes ∼15 minutes to acquire. Acquisition time for a local-region XFCT & CT with 30 projections, each with a size of 40 × 20 mm (200 μm pixels and 500 μm slice spacing, cf. Fig. 3a) is ∼1 hour, including overhead. As demonstrated here, a lower vertical sampling in the projection images for XFCT & CT can be chosen pragmatically so that the vertical range covers the region of interest while acquisition time is kept below a predefined limit.

B. Synthesis of MoO_2 Nanoparticles

The MoO_2 NPs are synthesized by a method described in detail elsewhere [4], [23]. Briefly, 300 mg ammonium heptamolybdate (AHM, $(NH_4)_6Mo_7O_{24}.4H_2O$, Sigma-Aldrich) is dissolved in 44 mL deionized water (DIW, 18 MΩ) and 20 mL ethanol (99.7%, Solveco) mixture. 1 g of PVP ($(C_6H_9NO)n$, 55 kDa, Sigma-Aldrich) is dissolved subsequently in the mixture and the solution is stirred for 30 min at room temperature. When the solution is clear 2 mL of 1 M HCl (Sigma-Aldrich) is added. The resulting solution is transferred to a 100 mL Teflon lined stainless steel autoclave and the hydrothermal reaction is performed at 180 °C for 18 h. The autoclave is cooled to room temperature and the precipitate is collected and washed by multiple centrifugations and re-dispersion in ultrapure water (Milli-Q®, Merck Millipore). Finally, we note that we use MoO_2 and not, e.g., Mo NPs due to their much higher stability in water.

C. Nanoparticle Characterization

Evaluation of NP size and morphology was performed with TEM (JEM-2100F, 200 kV, JEOL). 20 μL NP suspension was dropped on the TEM grid and air dried before analysis. For the size analysis, at least 350 NPs/clusters in different field of view are measured. Results showed that the NPs are spherical with a diameter of 5 ± 1.6 nm agglomerated in clusters with average diameter of 34 ± 9 nm (see Fig. 1c and Suppl. Fig. 4).

The crystallographic phase of the NPs was investigated by XRPD (Panalytical Xpert Pro alpha powder, PANalytical) with Cu K_α radiation, 1.5406 Å wavelength and scanning rate of 0.13°/min. Further, the crystallographic phase was confirmed by selected area electron diffraction in TEM. Results showed that the crystalline phase of the NPs is MoO_2 (see Suppl. Fig. 5).

Surface functional groups were identified by FT-IR (Thermo Fisher Scientific) in transmission mode. The sample in powder form was mixed with KBr in 1:9 ratio and the pellets were prepared using a manual pelletizer (Specac® mini-pellet press,

Sigma Aldrich). The quantitative estimation of PVP adsorbed on the surface of the NPs was done by thermogravimetric analysis (TGA) (TGA550, TA instruments). Results showed that polyvinylpyrrolidone (PVP) form a coating layer, visible in the TEM micrographs (Suppl. Fig. 4). This is also qualitatively confirmed by Fourier-transform infrared spectroscopy (FT-IR) (Suppl. Fig. 6). Furthermore, thermogravimetric analysis show that the PVP coating represents up to 27% of the weight of the analyzed sample (Suppl. Fig. 7).

By dynamic light scattering (DLS) and zeta potential analysis (Zetasizer Nano ZS90, Malvern) the hydrodynamic diameter and the surface charge of the NPs dispersed in DIW were assessed. The concentration of Mo in the NP stock solution was also quantified by inductively coupled plasma optical emission spectroscopy (iCAP 6000 series, Thermo Scientific). Results from DLS and zeta potential measurements confirmed the presence of PVP-MoO_2 clusters with an average hydrodynamic diameter of 59 ± 1.8 nm in DIW and a high colloidal stability due to the strong negative surface charge of -32 ± 0.8 mV (see Suppl. Table 1).

D. Limulus Amebocyte Lysate (LAL) Assay

Prior to the intravenous administration of NPs, the evaluation of lipopolysaccharides (LPS) contamination [24] was performed using the LAL assay Endosafe1-PTS for the stock NP solution and the sterile phosphate buffered saline (PBS) used for preparing the final suspensions. The evaluation was carried out according to the manufacturer's instructions by application of PTS cartridges with an assay sensitivity of 0.005 EU/mL. Results showed that the LPS values for the stock and PBS were below the maximum admissible limit of 0.1 EU/mL corresponding to the injected dose [25], [26].

E. Animal Studies

6-week-old female CIEA NOG mice (NOD.Cg-Prkdc^{scid} Il2rg^{tm1Sug}/JicTac; Taconic Biosciences, Denmark) were used in this study and were housed in a temperature (21 ± 1 °C) and humidity (55 ± 5%) controlled room under a 12-hour light/12-hour dark cycle, with free access to food and water ad libitum. Experimental animals ($n = 10$) were randomly assigned into three groups that were either intravenously injected with a suspension of 100 μL PBS with NPs at 1% Mo mass fraction ($n = 4$, further denoted as M1-M4), 100 μL PBS only (vehicle; $n = 3$) or were non-injected/non-scanned ($n = 3$). Injections were performed through the tail vein while mice were awake. The mice in the two first groups were imaged five times each (at 1 hour, 1 week, 2 weeks, 5 weeks, and 8 weeks post-injection) under identical circumstances using our laboratory XFCT arrangement described above. The mice were housed in mixed cages under the same conditions. All three experimental groups were used to investigate potential adverse effects from both NPs and x-ray exposure.

The health status of the mice was assessed according to the Karolinska Assessment Regulations. The following parameters were assessed on daily basis prior and during the full study length: body weight, general condition, eye condition, movement and posture, piloerection and fur condition, appetite, and respiration. Animal studies were performed with approval from the regional animal ethics committee of Northern Stockholm, Sweden (protocol number N50/16), according to institutional and European guidelines for animal handling and research (EU Directive 2010/63/EU for animal experiments). All efforts were made to follow the principles of the 3Rs in minimizing the number and suffering of animals used.

F. Anesthesia, Imaging Preparations and Post-Imaging Recovery

Prior to imaging, mice were anesthetized using room air mixed with isoflurane (Abbott, Sweden) at 4% during induction and 0.8-1.5% during maintenance anesthesia using the Univentor 410 Anesthesia Unit and Univentor 2010 Scavenger Unit (Agnthos, Sweden) coupled to an induction chamber placed on a heating pad that maintained body temperature at 37 °C. When mice no longer demonstrated the footpad pinch reflex, they were injected intraperitoneally with 0.5 mL saline solution (0.9% NaCl) heated to 37 °C to avoid dehydration during the imaging period. Eyes were covered by ophthalmic ointment (Oculentum simplex, APL, Sweden) to prevent corneal drying.

Following anesthetic induction, animals were then moved to a custom-designed animal bed and maintained under light general anesthesia by isoflurane administration through a small-footprint facemask. The mice were covered with a thin layer of soft heat-isolating foam and secured to the bed using non-sticking veterinary bandage to create the immobilization needed for minimal motion during imaging while still allowing an adequate respiration. The design of the bed allows the mice to be held in a vertical position during the full imaging period under anesthesia (typically 15-90 min depending on the type of imaging). See Suppl. Fig. 8 for photographs of the pre-imaging preparations as well as the custom-designed animal bed.

After imaging, the mice were placed in a recovery chamber placed on top of the heating pad (37 °C) to avoid hypothermia during recovery. Respiration, mobility, and reflexes were assessed until the mice were fully alert and mobile, upon which they were returned to their home cage.

G. Real-Time Monitoring of Vital Signs During Imaging

An important pre-requisite for longer *in vivo* imaging sessions is real-time monitoring of body temperature and respiration. This was performed using a dedicated small-animal monitoring system (MP160, BIOPAC Systems Inc, US). A pneumatic pillow connected to a differential pressure transducer was used as the respiratory sensor, placed between the abdominal region of the mouse and the vertical bed and thus allowing for sensitive real-time monitoring of respiratory movements. This way, the isoflurane concentration could be adjusted to maintain a respiratory rate of 110–130 breaths per minute (BPM) during the entire imaging period. Body temperature was monitored using a fast response thermistor and maintained at 37.2 °C (36.5–37.8 °C) during imaging using a controllable infrared heating lamp to avoid hypothermia.

Both sensors are visible in the transmission projection images (see, e.g., Fig. 2b).

H. Data Processing, Tomographic Reconstruction and 3D Visualization

Data processing following the image acquisition was performed in different steps. First, the relevant signals from the recorded spectrum at each pixel were extracted. The XRF signal was extracted by integrating the spectral region around the Mo K_α peak (see Fig. 1b). Furthermore, contribution from multiple Compton scattering was estimated and subtracted by integrating the energy bins on both sides of the K_α peak and then linearly correlating it with the magnitude of the main Compton peak at 23 keV (see Fig. 1b). The signal extraction algorithm is limited by photon statistics, meaning that in the case of few detected photons in the spectral regions of interest, background photons can be erroneously counted as XRF photons and vice versa. In other words, extracted XRF signal on the single-photon-level should be analyzed with caution. The transmission signal was obtained by integrating the whole transmitted spectrum for each pixel, as the transmitted x-ray photons are mostly around 24 keV. These steps are sufficient for 2D projection imaging (see, e.g., Fig 2a).

For XFCT & CT, projection images acquired at different rotations were tomographically reconstructed in to obtain 3D volumes (see, e.g., Fig 3a). CT reconstruction was performed using a standard filtered back-projection (FBP) algorithm. XFCT reconstruction was performed using our in-house developed self-absorption-correcting iterative reconstruction algorithms (for more details, see [4], [27]). All data processing was performed in Matlab (R2019b, MathWorks, US).

Visualizations of XFCT & CT (see Fig. 3a) was performed using a 3D rendering software (Amira 6.3, Thermo Fisher Scientific, US). Cubic interpolation was used in the 3D rendering to facilitate qualitative inspection. For the liver segmentation, anatomical knowledge of the liver morphology together with the CT reconstruction was used to manually separate the liver from the spleen and lungs in the XFCT reconstruction volumes at the best of our efforts.

I. Radiation Dose

Radiation dose for the two separate imaging procedures (whole-body projection images and XFCT & CT, respectively) was estimated using Monte Carlo simulations with our in-house developed and validated software [27]. In the simulations, the same imaging geometry seen in Fig. 1a was constructed with identical pencil-beam parameters (spectrum, flux, beam shape) and same acquisition settings as the ones used in the experiments. The anatomically correct and voxelized digital mouse phantom DIGIMOUSE [28] was used as the simulated object. During the simulation, deposited energies from absorbed x-ray photons were stored for each phantom voxel resulting in a 3D map of the absorbed radiation dose. Accounting for experimental overhead, average radiation dose from the projection images was then estimated to 1 mGy (soft-tissue: 0.8 mGy, bones: 3.4 mGy). For the combined XFCT & CT, the average radiation dose was estimated to 22 mGy (soft-tissue: 20 mGy, bones: 86 mGy). These values agreed with separate dose estimates acquired from the experimental CT images of each mouse, as described in an earlier publication [4].

J. Enzyme-Linked Immunosorbent Assay (ELISA)

As a marker of double-strand breaks from ionizing radiation, we measured phosphorylated-H2AX-Ser139 (γ-H2AX) and total H2AX levels in mouse liver extracts from the three experimental groups using an ELISA kit (RayBiotech Inc., US). Extracts from livers were chosen as the whole liver was exposed to x-rays during imaging, while other major organs such as the lungs were only partially exposed (cf. Fig. 3a). After the final imaging time point, while still under anesthesia all mice were immediately sacrificed through CO_2-inhalation followed by cervical dislocation. Extracts from mouse livers were collected and homogenized with a microtube homogenizer in lysis buffer (provided by the ELISA kit). Samples were sonicated for 1 min at a frequency of 22.5 kHz followed by centrifugation at $16000\times g$ for 10 minutes at 4 °C, the soluble fraction was collected, and the protein content was determined via bicinchoninic acid assay (BCA assay, Thermo Fisher Scientific, US). The assay was performed according to the manufacturer's instructions (see Suppl. Information for more details on the procedure).

K. Histological Analysis

At the end of the study, all mice were dissected according to protocol for histological analysis of major organs [29]. Lungs, heart, liver, spleen, kidneys, sternum, brain, and skin were collected and fixed in 4% formaldehyde for 24 hours and stored in 70% ethanol until processing and paraffin embedding. Sections of 4 μm thickness were obtained with a rotary microtome, then mounted on standard object glasses and automatically rehydrated and stained with hematoxylin and eosin (H&E) for analysis by light microscopy.

III. Results

A. Whole-Body XRF Projection Imaging

Fig. 2 demonstrates XRF projection imaging with 200×200 μm pixel size for *in vivo* whole-body localization of MoO_2 NP accumulations in mice. Pixel size in the images is equal to the acquisition step size. Fig. 2a shows projection images of the same mouse (M1) at the different imaging time points post NP injection. Due to the acquisition being slower than the typical breathing cycle of mice under anesthesia (scan speed ~20 mm/s, mouse width ~30 mm, breathing cycle ~2 Hz), some artifacts from respiratory motion are observed in the chest region. Acquisition time per projection was 15 minutes including ~25% overhead, resulting in an estimated radiation dose of 1 mGy (see Methods). We note that the very low levels of background signal (cf. Fig. 2b) allow imaging with high signal-to-background even when detecting only a few XRF photons.

As seen in Fig. 2a, NPs circulate and accumulate mainly in the lungs, liver, and spleen. The bladder shows strong signal

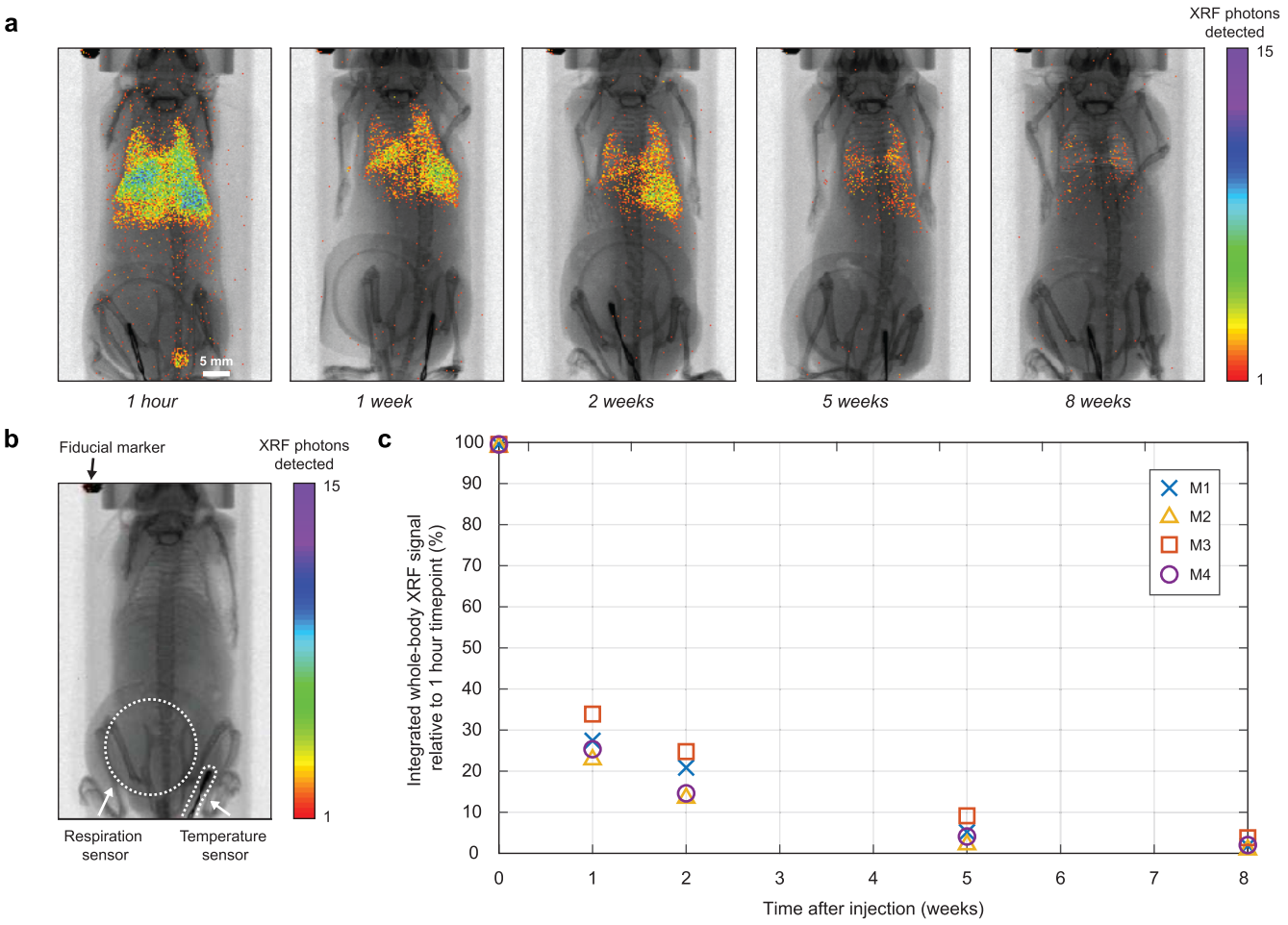

Fig. 2. Whole-body XRF projection imaging and NP clearance. **a**, XRF projection images (color) overlaid on x-ray transmission images (grayscale) of a mouse (M1) injected with MoO_2 NPs. Images of the same mouse were acquired at different time points post NP injection. The color bar shows the number of photons recorded in the Mo K_α peak after subtraction of estimated Compton background on a per-pixel basis. **b**, Same overlay for a mouse injected with vehicle (PBS) only, imaged 1-hour post injection. The respiration and temperature sensors are visible, together with the metal fiducial marker at the top left corner identifying the left side of the mouse. As the fiducial marker is a highly scattering object, there is a significantly higher probability of detecting scattered photons overlapping in energy with Mo XRF from the marker compared to from the rest of the animal bed. This explains the faint XRF signal observed from the fiducial marker. The sparsely detected XRF photons observed in other parts of the image are most likely background photons that have slipped through the XRF signal extraction algorithm, due to statistical limitations of the latter. **c**, Relative clearance of XRF signal over time for mice injected with NPs (M1-M4, n = 4). The total whole-body XRF signal was integrated for each time point and then divided by the value from the first time point for each mouse to determine the relative clearance.

at 1-hour post-injection, indicating possible urinary excretion of the NPs. A similar biodistribution pattern is observed in all mice receiving NP injections (see Suppl. Fig. 9). As the short pixel exposure times sets a limit on the sensitivity, no signal is seen in other organs such as kidney, brain, bone marrow etc. most likely due to lower accumulated NP concentrations.

Fig. 2c depicts the relative clearance of the whole-body XRF signal over time, which can be correlated to the clearance of the injected NPs. After 1-2 weeks, significant signal is still present in the lungs, liver, and spleen. After eight weeks the signal is close to the background level observed in mice injected with vehicle only (cf. Fig. 2b), confirming clearance of the NPs. Apart from the relative clearance of the XRF signal, we note that quantitative conclusions cannot be drawn from the projection images alone since effects such as self-absorption of XRF photons can only be modelled from tomographic data. The observed variation in XRF signal for the different mice is expected due to their variation in terms of size, weight, and individual biological response.

B. Quantitative XFCT of Liver

After acquiring whole-body projection images, we performed *in vivo* XFCT & CT of the mice at each time point. Fig. 3a shows a series of XFCT & CT acquired for the same mouse shown in Fig. 2a (M1). The liver was selected as a region of interest due to the major NP accumulation in the organ observed in the projection images. Each tomography is estimated to deliver ~22 mGy of radiation dose, thus each mouse accumulated a total of ~125 mGy during the whole five-scan eight-week study (including dose from projection images). We note that the accumulated radiation levels are within the range of a single typical preclinical micro-CT scan [30]. Furthermore, each tomography takes ~1 hour to acquire (including overhead).

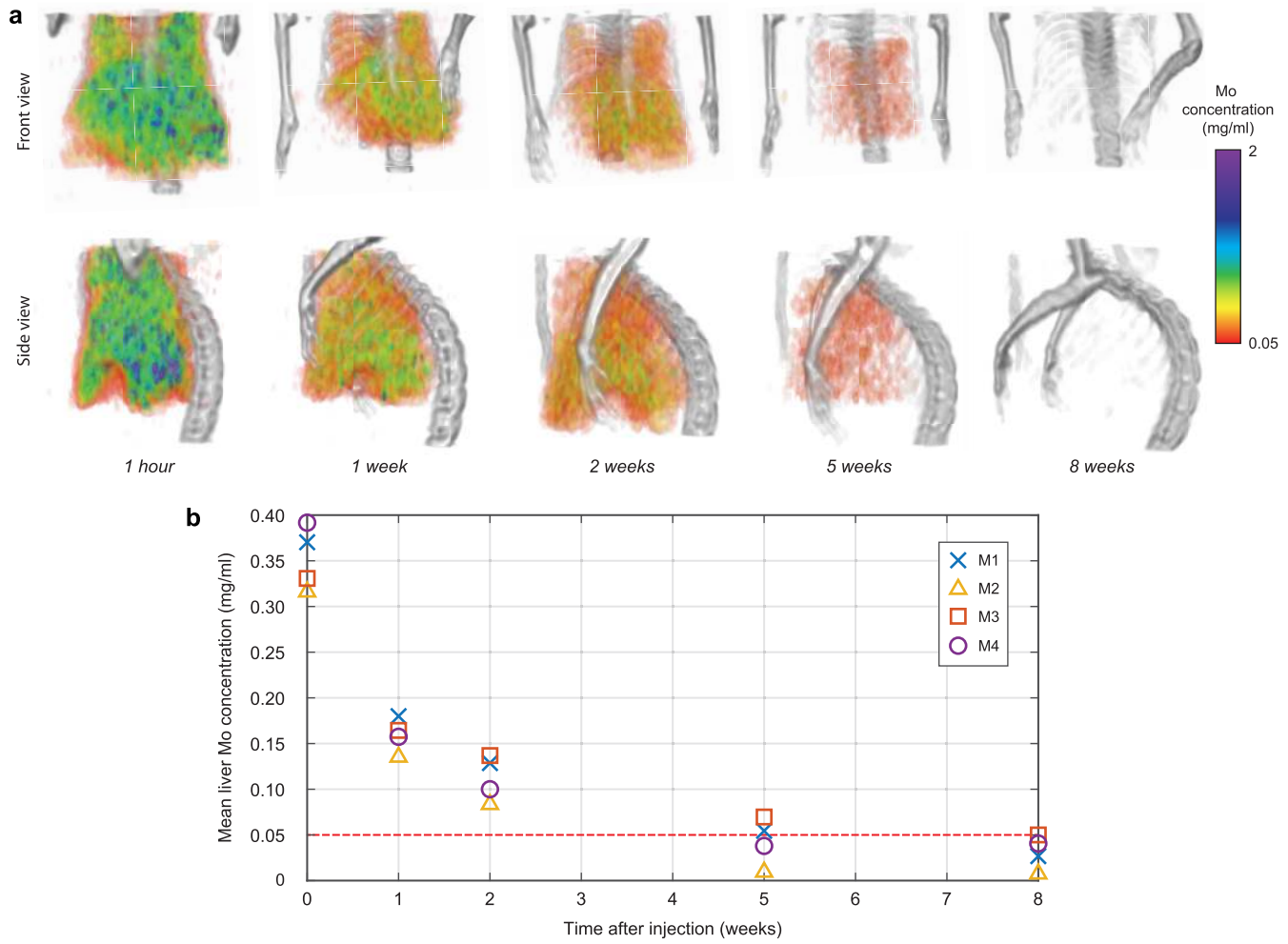

Fig. 3. Quantitative large-organ XFCT & CT. **a**, Liver-region XFCT & CT of the same mouse as in Fig. 2a (M1) at the different imaging time points. The acquired datasets were reconstructed, 3D-rendered (CT grayscale, XFCT color) and shown here in overlay. XFCT allows for quantitative estimations of NP accumulations (see color bar). Due to artifacts from respiratory motion, ribs are not always fully resolved in the CT reconstruction (most notably seen at the 8-week time point). **b**, Mean liver Mo concentration in mice injected with NPs (M1-M4) at the different imaging time points. Values were obtained through manual segmentation of the liver from the whole reconstruction volume (see **a**). The short pixel exposure times limit the detection sensitivity, here estimated to be around ~0.05 mg/mL (dashed red line), below which XRF signal from NP accumulations cannot be reliably separated from the background noise. This is due to the statistical limitations of our algorithms for XRF signal extraction and tomographic reconstruction at the single-photon level.

The reconstructed XFCT & CT volumes consist of 40 axial slices spaced by 500 μm. Each slice consists of 197 × 197 voxels with a voxel size of 200 μm for a total 3D volume of ~ 40 × 40 × 20 mm. While estimating the actual spatial resolution is challenging due to the anisotropic artifacts arising from respiratory motion, we note that phalanges and ribs as thin as 300 μm (measured post-mortem) are observed and quantified to 400 μm (i.e., horizontal width of two adjacent voxels) in the absorption CT. The simultaneous acquisition of XFCT & CT strongly suggests few-100-μm spatial resolution in the XFCT reconstruction as well. We note that the tomographic spatial resolution is currently limited by a combination of acquisition step size and artifacts from cardiorespiratory motion.

Our iterative XFCT reconstruction algorithms allow for quantitative determination of the locally accumulated NP concentration. The reconstructions in Fig. 3a show inhomogeneous distributions within the imaged volume including liver, spleen, and lungs at all time points. We note that the inhomogeneity might appear as a consequence of the low detected XRF signal creating a large variation among neighboring pixels (cf. Fig. 2a) and that the true distribution could potentially be more homogeneous. Nevertheless, in this case, we have previously shown with simulations that the mean value is still a good indicator of the true concentration in the volume of interest (liver in this case) [27]. By manual segmentation of the liver (see details in Methods), the mean accumulated liver Mo concentration for all mice injected with NPs (n = 4) is shown in Fig. 3b demonstrating exponential reduction in accumulated concentration over time. At a certain point the concentrations reach the detection limit of the imaging system, where the sparsely detected few-photon XRF signal (see eight-week projection in Fig. 2a) cannot be reliably reconstructed. Empirically we estimate this limit to ~0.05 mg/mL (or ~500 μM) of molybdenum. We note however that the detection limit can be improved linearly

(to first approximation) with increased pixel exposure time at the cost of increased radiation dose and longer scans.

Another benefit of the quantitative XFCT is the ability to estimate the fraction of injected NPs taken up by an organ of interest. This can give key insights into the biological clearance pathways of the NPs, and can further be used as a tool to quantify the impact of NP characteristics (e.g., size, surface, crystalline phase) on organ uptake. The estimation can be done by multiplying the mean NP concentration of an organ with the organ volume to acquire the accumulated NP mass and then compare with the injected dose. Since organ volume cannot be directly measured in a longitudinal *in vivo* study, we use the segmentation from the XFCT reconstruction to get an estimate of the liver volume at the first time point. The results reveal that ∼40-50% of the injected dose of NPs accumulate in the liver 1-hour post injection, and that the 1-week accumulation is around 20% of the injected dose (see Suppl. Table 2). As the organs were later extracted for histological analysis, no *ex vivo* validation of Mo accumulation in the livers was performed in this study. Nevertheless, we have previously shown that the results from our quantitative reconstruction algorithms agree with *ex vivo* measurements down to the order of 0.01 mg/mL of Mo using inductively coupled plasma mass spectrometry (ICP-MS) [4], a gold standard for quantitative analysis of trace elements.

C. Animal Well-Being, DNA Stability, and Histology

We evaluated the influence of NPs and x-ray imaging on animal well-being by assessing the health status of the mice post NP injection, as well as during the entire study. After injection with NPs, all mice (n = 4) exhibited normal active behavior similar to mice injected with vehicle only (n = 3). No difference in social activity or nesting behaviour could be observed between mice in the experimental groups in the daily assessment performed during the full eight-week duration of the study. Furthermore, we assessed fur condition, eye condition, appetite, piloerection, movement, posture, and respiration. During the eight-week study, all the aforementioned points were normal for all mice. Weight curves showed no significant difference in growth between all three groups during the study (see Suppl. Fig. 10).

Adverse effects associated with the XFCT imaging was evaluated with emphasis on respiratory behavior and temperature management. Assessment was performed during the pre-imaging anesthetic induction phase, during imaging as well as during the post-imaging recovery through monitoring of respiration and temperature trends using sensors together with visual behavioral inspection. No difference in respiration or temperature management could be observed between mice injected with NPs and vehicle only. All mice fully recovered (awake, alert, and mobile) within approximately 1 minute post-imaging upon removal from the anesthetic gas.

Ionizing radiation induces different types of DNA damage including double-strand breaks (DSBs) which is a serious lesion that can initiate genomic instability and cell death [31], [32]. The combined radiation dose in this study (∼1 + 22 mGy per time point) is well within the range of conventional preclinical CT [30]. Nevertheless, we analyzed the possible impact of x-ray exposure on DNA stability by comparing the experimental groups exposed to x-rays (n = 7) with the non-exposed group (n = 3). To this end, we measured the levels of phosphorylated-H2AX-Ser139 (γ-H2AX) as a marker of DSBs [33], [34] in liver extracts of the mice at the end of the study. No significant increase in γ-H2AX was detected in the two animal groups exposed to ionizing radiation (vehicle- and NP-injected mice) compared to the third control group (cf. Suppl. Fig. 11), which further confirms that our radiation dose is suitable for longitudinal *in vivo* studies.

Histologic assessment of the major organs (lungs, heart, liver, spleen, kidneys, sternum, brain, and skin) from all mice (n = 10) was performed at the end of the study. Importantly, no morphological abnormalities such as fibrosis, necrosis, or other general structural changes were observed in any of the major organs. Notably, in two out of four mice injected with NPs evidence of pulmonary thrombosis was observed (in M3 in the pulmonary artery branch, in M4 a possible vascular intramural plaque), as well as a thrombus in the right ventricular lumen in a third mouse (M2) as shown in Suppl. Fig. 12. Although routine histology provides limited insight in the cause and full extent of thrombus formation, thrombi are of chronic nature and are organized by fibroblasts. Their presence indicates that a possible causal relation with the NPs may be limited to the initially high concentration in the blood. The vascular changes were not occlusive, and we did not note clinical symptoms such as laboured respiration or signs of increased stress in any of the mice throughout the eight-week study. Still, further investigation is needed to establish the causal relation between the thrombi formation and the MoO_2 NPs.

IV. Discussion

We have shown that laboratory x-ray fluorescence computed tomography (XFCT) with high spatial resolution has potential for longitudinal studies *in vivo* (i.e., repeated imaging of the same animal over time) with scan times (∼1 hour) and radiation dose (<25 mGy) in range for routine preclinical imaging. In this proof-of-principle longitudinal study we performed tail-vein-injection of in-house-synthesized MoO_2 NPs. We demonstrate few-100-μm spatial resolution *in vivo* XFCT imaging at different time points with a Mo sensitivity down to the order of 10^{-2} mg/mL (or 100 μM). We note that our method combines the spatial resolution and penetration depth of the morphology-sensitive x-ray imaging with the molecular contrast of PET, SPECT and emerging optical methods [2] and thereby bridges the resolution gap between molecular and morphological biomedical imaging.

During the course of our eight-week study, we evaluated animal well-being by daily qualitative assessment of the mice (n = 10). Social behavior, activity, appetite, fur condition, eye condition, piloerection, posture and respiration were all normal for all mice associated with the different experimental groups during the whole study. Post-mortem analysis of DNA-integrity in liver extracts revealed no increase in γ-H2AX from x-ray exposure, confirming that the radiation dose from our

imaging arrangement is suitable for preclinical studies. DSB measurements in blood could provide a more sensitive measure of acute effects from ionizing radiation and will be used in our future studies to further investigate the effect of x-ray exposure on DNA stability.

XRF projection images show that the MoO_2 NPs accumulate mainly in the lungs, liver, and spleen at 1-hour post injection. Residual accumulation after one week indicates that the MoO_2 NPs avoid rapid renal clearance, as expected from the size distribution of the NP clusters (∼59 nm hydrodynamic diameter, cf. Suppl. Table 1) [35]. The strong liver signal indicates uptake mainly by macrophages (Kuppfer cells) in the mononuclear phagocyte system [36]. The longitudinal imaging suggests that nearly all of the MoO_2 NPs are excreted after eight weeks. However, as regards the NP dynamics and the detailed excretion pathways much remains to be investigated. The *in vitro* stability of the NPs in different media (water, PBS, serum and blood) are under current investigation, and should provide a better understanding of NP aggregation and dissolution in biological systems.

Histological examination of extracted organs following the end of the eight-week study showed no alteration of tissue structure overall compared to the control group. However, vascular changes expressed in formation of thrombi were observed in mice injected with NPs, while not in other mice. We note that this is a known effect related to the interaction between nanomaterials and the coagulation system [37], [38]. For our future studies we will adopt strategies identified in the literature for increasing the hemocompatibility of NPs [39], [40] if necessary combined with anti-coagulants, a well-established clinical procedure for thrombosis prevention (cf., e.g., [41]).

Our pencil-beam-based XFCT enables high resolution imaging despite its intrinsically slow sequential data acquisition. Nominally pinhole-based systems in XFCT offer parallel data acquisition but at the price of spatial resolution being limited by the pinhole itself. Just as in pinhole-SPECT [42], high-resolution XFCT pinhole imaging requires small-diameter apertures, thus, sacrificing sensitivity for resolution. Our pencil-beam approach offers higher spatial resolution (>5-10×), lower radiation dose (>4-20×) and higher sensitivity (>25-30×) than state-of-the-art pinhole-based *in vivo* XFCT at comparable scan times [21], [22].

The maximum attainable spatial resolution in our present laboratory XFCT arrangement is limited by the pencil-beam diameter. This is a technical limitation, contrary to PET or the optical methods, which are resolution-limited by fundamental positron physics or unavoidable tissue scattering of optical photons, respectively. Theoretically our present XFCT arrangement allows observation of features as small as the acquisition pixel size (currently 200 μm) [27]. Example of such features could be early-stage tumors. The requirement is that a sufficiently high concentration of Mo accumulates in the feature, which can be achieved in the future with improved high-specificity active-targeted NPs. Technically, 100 μm step sizes are possible in our current arrangement due to the ∼100 μm focus diameter of the pencil-beam (cf. Suppl. Fig. 2). However, shorter step sizes results in longer scan times if pixel exposure times and sensitivity are to be kept. In order to make *in vivo* XFCT with 100 μm spatial resolution practically feasible, we will increase the XRF detector area to compensate shorter pixel exposure times (5 ms) with a larger detection solid angle. This results in preserved sensitivity and scan times while spatial resolution is improved, and radiation dose reduced. Future work on the laboratory arrangement is directed towards *in vivo* 100-μm spatial resolution XFCT with acceptable sensitivity using this approach. At this length scale image artifacts arising from cardiorespiratory motion will be increasingly important to address, preferably through prospectively gated image acquisition.

While the 1-hour XFCT scan time demonstrated here is a time-frame acceptable for preclinical investigations, quicker scans would open for new types of studies such as dynamic monitoring of NP biological pathways. Using our current approach, maximum acquisition speed is limited by the speeds at which the mice can be rotated and translated without inducing discomfort (current 10 ms pixel exposure times and 200 μm pixel sizes result in 20 mm/s translations). These issues can be solved with a rotating gantry arrangement in the future.

With its combination of spatial resolution, low radiation dose, molecular sensitivity, and applicability to longitudinal *in vivo* studies, the pencil-beam XFCT arrangement described here should find applications in preclinical studies on cancer (e.g., early detection), tumor biology (e.g., volume, vascularization, or molecular marker identification), or in drug development and drug screening experiments. This can be achieved using NPs surface-coated with, e.g., proteins for active receptor targeting, which we are currently investigating. Although it is too early to speculate about clinical applications, we note that the low dose and short exposure time already demonstrated would make it applicable to thin clinical objects like breast or hand. Imaging thicker body parts will require harder x-rays, NPs based on heavier elements, and new detectors.

Acknowledgment

The authors would like to thank Nyosha Alikhani for discussions and support during the initial phase of the study and Tarja Schröder (Karolinska Institute core facility for Morphological Phenotype Analysis) for histotechnical handling.

References

[1] G. C. Kagadis, G. Loudos, K. Katsanos, S. G. Langer, and G. C. Nikiforidis, "*In vivo* small animal imaging: Current status and future prospects," *Med. Phys.*, vol. 37, no. 12, pp. 6421–6442, Nov. 2010.

[2] T. F. Massoud, "Molecular imaging in living subjects: Seeing fundamental biological processes in a new light," *Genes Develop.*, vol. 17, no. 5, pp. 545–580, Mar. 2003.

[3] H. M. Hertz, J. C. Larsson, U. Lundström, D. H. Larsson, and C. Vogt, "Laboratory X-ray fluorescence tomography for high-resolution nanoparticle bio-imaging," *Opt. Lett.*, vol. 39, no. 9, pp. 2790–2793, 2014.

[4] J. C. Larsson *et al.*, "High-spatial-resolution X-ray fluorescence tomography with spectrally matched nanoparticles," *Phys. Med. Biol.*, vol. 63, no. 16, Aug. 2018, Art. no. 164001.

[5] Y. Kuang, G. Pratx, M. Bazalova, B. Meng, J. Qian, and L. Xing, "First demonstration of multiplexed X-ray fluorescence computed tomography (XFCT) imaging," *IEEE Trans. Med. Imag.*, vol. 32, no. 2, pp. 262–267, Feb. 2013.

[6] B. R. Smith and S. S. Gambhir, "Nanomaterials for *in vivo* imaging," *Chem. Rev.*, vol. 117, no. 3, pp. 901–986, Feb. 2017.

[7] J. F. Hainfeld, D. N. Slatkin, T. M. Focella, and H. M. Smilowitz, "Gold nanoparticles: A new X-ray contrast agent," *Brit. J. Radiol.*, vol. 79, no. 939, pp. 248–253, Mar. 2006.

[8] O. Rabin, J. M. Perez, J. Grimm, G. Wojtkiewicz, and R. Weissleder, "An X-ray computed tomography imaging agent based on long-circulating bismuth sulphide nanoparticles," *Nature Mater.*, vol. 5, no. 2, pp. 118–122, Feb. 2006.

[9] M. Shilo, T. Reuveni, M. Motiei, and R. Popovtzer, "Nanoparticles as computed tomography contrast agents: Current status and future perspectives," *Nanomedicine*, vol. 7, no. 2, pp. 257–269, Feb. 2012.

[10] W. Eck, A. I. Nicholson, H. Zentgraf, W. Semmler, and S. Bartling, "Anti-CD4-targeted gold nanoparticles induce specific contrast enhancement of peripheral lymph nodes in X-ray computed tomography of live mice," *Nano Lett.*, vol. 10, no. 7, pp. 2318–2322, Jul. 2010.

[11] J. F. Hainfeld, M. J. O'Connor, F. A. Dilmanian, D. N. Slatkin, D. J. Adams, and H. M. Smilowitz, "Micro-CT enables microlocalisation and quantification of Her2-targeted gold nanoparticles within tumour regions," *Brit. J. Radiol.*, vol. 84, no. 1002, pp. 526–533, Jun. 2011.

[12] D. Peer, J. M. Karp, S. Hong, O. C. Farokhzad, R. Margalit, and R. Langer, "Nanocarriers as an emerging platform for cancer therapy," *Nature Nanotechnol.*, vol. 2, no. 12, p. 751, 2007.

[13] Z. Cheng, A. Al Zaki, J. Z. Hui, V. R. Muzykantov, and A. Tsourkas, "Multifunctional nanoparticles: Cost versus benefit of adding targeting and imaging capabilities," *Science*, vol. 338, no. 6109, pp. 903–910, Nov. 2012.

[14] G. Hong, A. L. Antaris, and H. Dai, "Near-infrared fluorophores for biomedical imaging," *Nature Biomed. Eng.*, vol. 1, no. 1, pp. 1–22, Jan. 2017.

[15] L. Mezzanotte, M. van't Root, H. Karatas, E. A. Goun, and C. W. G. M. Löwik, "*In vivo* molecular bioluminescence imaging: New tools and applications," *Trends Biotechnol.*, vol. 35, no. 7, pp. 640–652, Jul. 2017.

[16] M. Ahmad, G. Pratx, M. Bazalova, and L. Xing, "X-ray luminescence and X-ray fluorescence computed tomography: New molecular imaging modalities," *IEEE Access*, vol. 2, pp. 1051–1061, 2014.

[17] S. K. Cheong, B. L. Jones, A. K. Siddiqi, F. Liu, N. Manohar, and S. H. Cho, "X-ray fluorescence computed tomography (XFCT) imaging of gold nanoparticle-loaded objects using 110 kVp X-rays," *Phys. Med. Biol.*, vol. 55, no. 3, p. 647, Jan. 2010.

[18] M. Ahmad, M. Bazalova-Carter, R. Fahrig, and L. Xing, "Optimized detector angular configuration increases the sensitivity of X-ray fluorescence computed tomography (XFCT)," *IEEE Trans. Med. Imag.*, vol. 34, no. 5, pp. 1140–1147, May 2015.

[19] N. Manohar, F. J. Reynoso, P. Diagaradjane, S. Krishnan, and S. H. Cho, "Quantitative imaging of gold nanoparticle distribution in a tumor-bearing mouse using benchtop X-ray fluorescence computed tomography," *Sci. Rep.*, vol. 6, no. 1, Apr. 2016, Art. no. 22079.

[20] T. Sasaya, N. Sunaguchi, K. Hyodo, T. Zeniya, and T. Yuasa, "Multi-pinhole fluorescent X-ray computed tomography for molecular imaging," *Sci. Rep.*, vol. 7, no. 1, pp. 1–12, Dec. 2017.

[21] S. Zhang, L. Li, J. Chen, Z. Chen, W. Zhang, and H. Lu, "Quantitative imaging of Gd nanoparticles in mice using benchtop cone-beam X-ray fluorescence computed tomography system," *Int. J. Mol. Sci.*, vol. 20, no. 9, p. 2315, May 2019.

[22] S. Jung *et al.*, "Dynamic *in vivo* X-ray fluorescence imaging of gold in living mice exposed to gold nanoparticles," *IEEE Trans. Med. Imag.*, vol. 39, no. 2, pp. 526–533, Feb. 2020.

[23] J. Dou and H. C. Zeng, "Targeted synthesis of silicomolybdic acid (keggin acid) inside mesoporous silica hollow spheres for Friedel–Crafts alkylation," *J. Amer. Chem. Soc.*, vol. 134, no. 39, pp. 16235–16246, Oct. 2012.

[24] M. A. Dobrovolskaia, D. R. Germolec, and J. L. Weaver, "Evaluation of nanoparticle immunotoxicity," *Nature Nanotechnol.*, vol. 4, no. 7, pp. 411–414, Jul. 2009.

[25] P. Malyala and M. Singh, "Endotoxin limits in formulations for preclinical research," *J. Pharmaceutical Sci.*, vol. 97, no. 6, pp. 2041–2044, Jun. 2008.

[26] *Guidance for Industry: Pyrogen and Endotoxins Testing: Questions and Answers*, U.S. Food Drug Admin., White Oak, MD, USA, 2012. [Online]. Available: https://www.fda.gov/regulatory-information/search-fda-guidance-documents/guidance-industry-pyrogen-and-endotoxins-testing-questions-and-answers

[27] K. Shaker, J. C. Larsson, and H. M. Hertz, "Quantitative predictions in small-animal X-ray fluorescence tomography," *Biomed. Opt. Express*, vol. 10, no. 8, pp. 3773–3788, 2019.

[28] B. Dogdas, D. Stout, A. F. Chatziioannou, and R. M. Leahy, "Digimouse: A 3D whole body mouse atlas from CT and cryosection data," *Phys. Med. Biol.*, vol. 52, no. 3, p. 577, 2007.

[29] C. Antal, M. Teletin, O. Wendling, M. Dgheem, J. Auwerx, and M. Mark, "Tissue collection for systematic phenotyping in the mouse," *Current Protocols Mol. Biol.*, vol. 80, no. 1, p. 29, Oct. 2007.

[30] S. K. Carlson, K. L. Classic, C. E. Bender, and S. J. Russell, "Small animal absorbed radiation dose from serial micro-computed tomography imaging," *Mol. Imag. Biol.*, vol. 9, no. 2, pp. 78–82, Feb. 2007.

[31] J. Vignard, G. Mirey, and B. Salles, "Ionizing-radiation induced DNA double-strand breaks: A direct and indirect lighting up," *Radiotherapy Oncol.*, vol. 108, no. 3, pp. 362–369, Sep. 2013.

[32] S. P. Jackson and J. Bartek, "The DNA-damage response in human biology and disease," *Nature*, vol. 461, no. 7267, pp. 1071–1078, Oct. 2009.

[33] W. M. Bonner *et al.*, "γ H2AX and cancer," *Nature Rev. Cancer*, vol. 8, no. 12, pp. 957–967, 2008.

[34] C. E. Redon, J. S. Dickey, W. M. Bonner, and O. A. Sedelnikova, "γ -H2AX as a biomarker of DNA damage induced by ionizing radiation in human peripheral blood lymphocytes and artificial skin," *Adv. Space Res.*, vol. 43, no. 8, pp. 1171–1178, Apr. 2009.

[35] E. Blanco, H. Shen, and M. Ferrari, "Principles of nanoparticle design for overcoming biological barriers to drug delivery," *Nature Biotechnol.*, vol. 33, no. 9, p. 941, 2015.

[36] S. M. Moghimi, A. C. Hunter, and J. C. Murray, "Long-circulating and target-specific nanoparticles: Theory to practice," *Pharmacol. Rev.*, vol. 53, no. 2, pp. 283–318, 2001.

[37] J. Simak and S. De Paoli, "The effects of nanomaterials on blood coagulation in hemostasis and thrombosis," *Wiley Interdiscipl. Rev., Nanomed. Nanobiotechnol.*, vol. 9, no. 5, p. e1448, Sep. 2017.

[38] P. Urbán, N. J. Liptrott, and S. Bremer, "Overview of the blood compatibility of nanomedicines: A trend analysis of *in vitro* and *in vivo* studies," *Wiley Interdiscipl. Rev., Nanomed. Nanobiotechnol.*, vol. 11, no. 3, p. e1546, May 2019.

[39] A. N. Ilinskaya and M. A. Dobrovolskaia, "Nanoparticles and the blood coagulation system. Part II: Safety concerns," *Nanomedicine*, vol. 8, no. 6, pp. 969–981, Jun. 2013.

[40] E. Fröhlich, "Action of nanoparticles on platelet activation and plasmatic coagulation," *Current Med. Chem.*, vol. 23, no. 5, pp. 408–430, Feb. 2016.

[41] R. Engelman *et al.*, "The society of thoracic surgeons, the society of cardiovascular anesthesiologists, and the American society of ExtraCorporeal technology: Clinical practice guidelines for cardiopulmonary bypass—Temperature management during cardiopulmonary bypass," *Ann. Thoracic Surg.*, vol. 100, no. 2, pp. 748–757, Aug. 2015.

[42] A. Rahmim and H. Zaidi, "PET versus SPECT: Strengths, limitations and challenges," *Nucl. Med. Commun.*, vol. 29, no. 3, pp. 193–207, Mar. 2008.